

## Correcting spatial distortion in histological images

Michael S. Breen<sup>a</sup>, Tanya L. Lancaster<sup>a</sup>, David L. Wilson<sup>a,b,\*</sup>

<sup>a</sup>Department of Biomedical Engineering, Case Western Reserve University, Cleveland, OH 44106, USA

<sup>b</sup>Department of Radiology, University Hospitals of Cleveland & Case Western Reserve University, 2074 Abington Road, Cleveland, OH 44106, USA

Received 1 December 2004; accepted 11 April 2005

---

### Abstract

We described an interactive method for correcting spatial distortion in histology samples, applied them to a large set of image data, and quantitatively evaluated the quality of the corrections. We demonstrated registration of histology samples to photographs of macroscopic tissue samples and to MR images. We first described methods for obtaining corresponding fiducial and anatomical points, including a new technique for determining boundary correspondence points. We then describe experimental methods for tissue preparation, including a technique for adding color-coded internal and boundary ink marks that are used to validate the method by measuring the registration error.

We applied four different transformations with internal and boundary correspondence points, and measured the distance error between other internal ink fiducials. A large number of boundary points, typically 20–30, and at least two internal points were required for accurate warping registration. Interior errors with the transformation methods were ordered: thin plate spline (TPS)  $\approx$  non-warping  $\ll$  triangle warping  $<$  polynomial warping. Although non-warping surprisingly gave the lowest interior distance error ( $0.5 \pm 0.3$  mm), TPS was more robust, gave an insignificantly greater error ( $0.6 \pm 0.3$  mm) and much better results near boundaries where distortion was more evident, and allowed us to correct torn histology samples, a common problem. Using the method to evaluate RF thermal ablation, we found good zonal correlation between MR images and corrected histology samples. The method can be practically applied to this and other emerging applications such as in vivo molecular imaging.

© 2005 Elsevier Ltd. All rights reserved.

**Keywords:** Medical image processing; Image registration; Tissue typing; Interventional magnetic resonance imaging; Thermal ablation; Histology

---

### 1. Introduction

We are developing methods to enable the comparison of medical image data to corresponding histological data [1,2]. This paper describes a critical aspect: the correction of distortion caused by histological processing. There are many instances where one wants to relate medical image data to the cellular response, as determined from histological samples, and we will describe some examples from our institution. First, there is much experience in radiofrequency (RF) ablation of tissue, typically cancerous tumors, under interventional magnetic resonance imaging (iMRI) guidance [3–7]. With regard to RF ablation, magnetic

resonance imaging (MRI) can intermittently acquire temperature images during heating and structural lesion images during and after heating. Our goal is to quantitatively relate MR image measurements to tissue damage as seen histologically [1]. Second, we are attempting to correlate single positron emission computed tomography (SPECT) images using a monoclonal antibody imaging agent with tumor in the prostate by correlating the medical images with histology [8]. Third, we are using medical images to characterize in vivo drug release from a new device for localized, controlled drug release [9]. Future experiments in drug response will require histological correlation. There are many other potential applications. Notably, as medical imaging techniques are used to study in vivo molecular biology using new agents [10,11], histological validation will be critical.

As an example application, we will review the application where MR images of thermal ablation are compared to tissue response [4,5,12–15]. Only one report uses registration, and it is a two-dimensional (2D) method [14]. Others simply measure thermal lesion diameters or

---

\* Corresponding author. Address: Department of Biomedical Engineering, Case Western Reserve University, Cleveland, OH 44106, USA. Tel.: +1 216 368 4099; fax: +1 216 368 4969.

E-mail address: dlw@case.edu (D.L. Wilson).

lengths in 2D MR and tissue images [4,5,12,15]. Such methods are limited by ones ability to accurately determine corresponding image slices and by the applicability of simple length measures to capture what might be a complicated three-dimensional (3D) geometry, especially in the event of multiple ablation sites. Recognizing these limitations, we are developing a 3D method consisting of a 3D rigid body registration of MR to macroscopic tissue photographs using needle fiducials followed by a 2D warp of histological sections to the macroscopic tissue photographs to correct deformation that occurs during tissue processing [1,2]. This method allows us to compare MR thermal ablation images to the corresponding histology, and hence compare MR measurements to cell death and damage. Correction of spatial distortion in histological processing is a critical step in this process.

There are methods in the literature that attempt to correct spatial distortion found in histology images. A multi-resolution, mutual information approach with thin plate spline (TPS) warping was used by Likar and Pernus [16] to align pairs of high magnification histology slides having different stains in order to classify skeletal muscle fibers. Another mutual information-based approach with TPS warp was used for correcting spatial distortions in rat brain autoradiographs [17]. This technique corrected autoradiographs to the corresponding block face image obtained during cryosectioning. Locations of six control point pairs in the 2D images were optimized for a mutual information similarity measure, and the final control point locations were used for a TPS warp. Jacobs et al. [18] used a surface-based, ‘head in hat,’ 3D method to register rat brain histology and MR images. To correct for spatial distortion in the histological images, they warped 2D MR images to the histological samples. Radial correspondence from a center of mass was assumed to obtain corresponding points for the TPS transformation. As part of the human brain-mapping project, cellular histology data from human brains have been mapped to medical images. As reviewed by Toga et al. [19], histology images were warped to match 2D block face images from cryosectioned brain volumes, which in turn were matched to medical images and/or atlases. Several warping methods have been applied including elastic surface and viscous fluid-based deformations [20]. Others have applied similar methods for brain mapping [21,22].

Although the above methods would probably work for some of our data, we desired a more flexible approach suitable for a wide variety of tissues, spatial distortions, missing image data due to tissue tearing, and a variety of image pairs, including MR to histology. Some methods use relatively few control points, and we require many, especially at edges, in order to correct the spatial distortions found there. This is particularly an issue because thermal ablations are often applied near the surface of an organ. Although radial correspondence is reasonable to apply in the brain, it is not generally applicable. Gray-scale matching methods such as mutual information require at least

somewhat similar features, and the brain data used by many have an abundance of such features. MR images, especially those of rabbit thigh muscle, have very few features suitable for matching to histology, and the most prominent feature in histology, the edges, often do not exist in the MR image counterparts. Moreover, our goal is to determine if lesions seen in MR match those in histology. A method that warps an image to match the lesion would invalidate the experiment. Finally, we often find histology samples with missing sections due to tearing, probably because ablations can change the consistency of the tissue sample and a histology section of a tissue such as muscle can contain anatomical boundaries that separate during processing. For these and other reasons, we developed a new 2D method, which can be used interactively in a wide variety of preparations.

Relatively little validation work has been done to show that histological images are correctly transformed. Visual methods such as contour overlays and difference images are most often employed [16,19,21,22]. Image gray level measures such as mutual information can be examined [17]. Jacobs et al. [18] show that stroke lesion areas from MR and histology correlate better with warping than without warping. In those cases where point anatomical landmarks are visible in both image pairs, one could estimate error, but this has not been widely reported.

In this paper, we describe interactive methods for correcting spatial distortion in histology samples, apply them to a large set of image data, and quantitatively evaluate the quality of the corrections. We first describe methods for obtaining correspondence points, including a new technique for determining boundary correspondence points. Four different warping transformations are described. We then describe experimental methods for tissue preparation, including a technique for adding color-coded internal and boundary ink marks that are used to validate the method by measuring the transformation error. In Section 4, from a variety of experiments including ones with practical problems like incomplete boundaries and torn tissue sections, we determine the best algorithm and its accuracy. Finally, we apply the method to an example RF thermal ablation experiment.

## 2. Warping registration method

We now give a brief overview of our method for transforming a spatially distorted, 2D histology image to spatially match a reference image. Most often, the reference image is a photograph of a macroscopic tissue image prior to histological preparation, but it can also be a 2D MR or computed tomography (CT) image. The method works by matching corresponding points between the two images as obtained from manual entry or automatic processing of the border. Given a set of corresponding points, we then apply one of a variety of transformation methods to match

the images. Once transformations have been applied, registration quality is evaluated by inspection using a variety of visualization tools and by an error metric consisting of the average distance between corresponding points. All software was developed using IDL (Interactive Data Language, Research Systems, Inc., Boulder, CO). As described later, the method also includes experimental aspects including careful tissue handling and the inclusion of ink fiducial points.

### 2.1. Creating correspondence points

Correspondence points are obtained in two ways, and Fig. 1 contains a flow chart of the process. In the first approach (lower left of Fig. 1), we manually identify points from internal anatomical landmarks such as blood vessels or from fiducial marks such as needle tracks. In addition, we

add ink fiducial marks by inserting pins dipped in ink into the macroscopic tissue sections. In our computer program, the user identifies corresponding point pairs interactively from two images in a side-by-side display, as described later.

The second approach for obtaining corresponding points (top of Fig. 1) uses identifiable boundary segments. Corresponding boundary end points are identified either from an anatomical landmark or, more commonly, from an ink mark. Once these are identified, the boundaries are delineated using a live-wire segmentation algorithm [23,24] briefly described below. The output of this algorithm is a list of pixel locations identifying the boundary segment from start to end. Since the endpoints of the boundary segment match in both images and the path between the endpoints along the border should be similar for both images, we simply divide the corresponding segments into a set of corresponding equidistant points digitized to the nearest pixel along the boundary. The live-wire algorithm and the distance calculation are done using a four connected neighborhood in order to speed processing. The distance is simply obtained by summing the number of pixels along the boundary. Typically, this process is repeated for three to seven boundary segments. Corresponding boundary points are added to those from manual entry to create a large list of corresponding points.

The segmentation of border segments is accomplished using a modified live-wire algorithm [23]. To apply live-wire segmentation, the user inputs a starting point and, as the cursor is moved along the boundary, the path snaps to the edge like a 'live-wire' until a final end point is chosen and segmentation is completed. This is a natural choice for our interactive method requiring segmentation of identifiable boundary segments. Inputs to the algorithm consist of a starting point and a gradient magnitude-based cost map of the image. Cost maps for histological images are created by applying a Sobel filter to the median filtered green channel. A  $3 \times 3$  median filter is applied three to five times to fill small spaces that naturally occur in histology samples while preserving boundary edges. For the color macroscopic tissue image, a Sobel filter is applied to the red, green, and blue channels, and the maximum gradient magnitude of the three is used as the cost at each pixel in the image. Cost maps are calculated once and stored to speed the interactive portion of the algorithm. A four-connected, 2D dynamic programming algorithm is used to determine the minimum cost and its path from the starting point to any possible end point contained within a region of interest in the image. Once this is completed, as the user interactively moves the cursor to potential end pixels, the program can quickly backtrack to the starting point giving the impression of a live-wire. If the path strays from the desired boundary, the additional low cost control points can be added to anchor the path to the boundary.

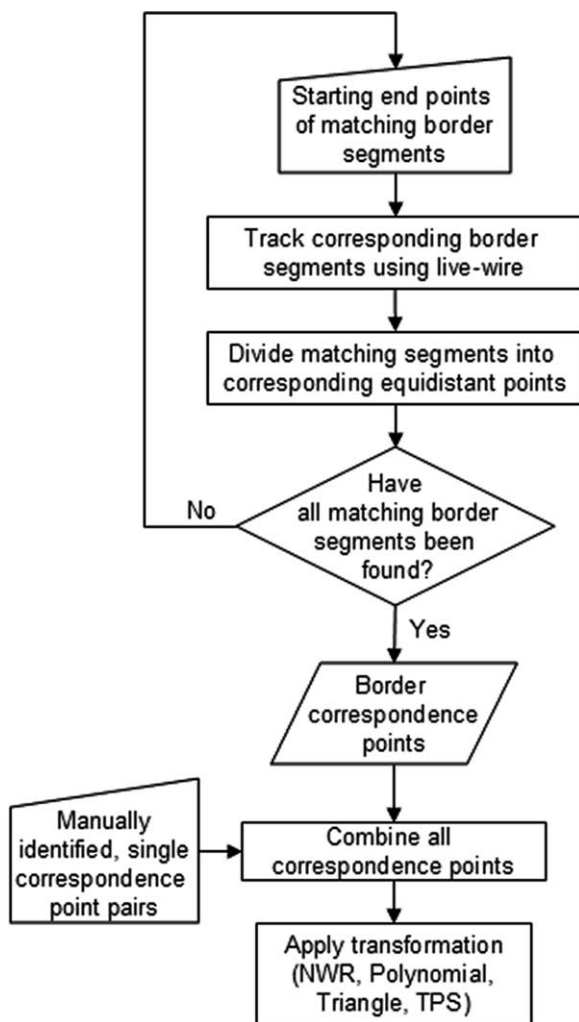


Fig. 1. Flow chart for determining correspondence points. The user identifies starting points and then segments corresponding borders using live-wire. The matching borders are then divided into a set of equidistant correspondence points. These border points are added to manually identified points creating a final list used for all transformations.

## 2.2. Image visualization and interaction

We developed an interactive software program in IDL that allowed the user to identify corresponding points by manual entry or by the interactive live-wire approach. Immediately after the user selects images to load, the program calculates cost maps for the live-wire algorithm. To make identification of correspondence points easier, images can be rotated in increments of 90° to roughly align them. Side-by-side display windows are used for easy image comparison.

Typically, most corresponding points are identified along the boundaries of the tissue. Live-wire is used to provide greater flexibility, consistency, and a faster segmentation as opposed to a manual approach. An interactive path is displayed from the cursor to a user selected starting point. This path often snaps immediately to the boundary of the tissue, making segmentation of the border simple and consistent across users. In the event that a path strays from a boundary, anchor points can be added. Anchor points are sometimes necessary for irregular boundaries in a torn area of a histology image. Following identification of corresponding points, transformations can be applied to the histology image. An additional window pops up with the final transformed image for easy visual comparison to the reference. A decision is then made to save the image, add additional corresponding points, or try an alternate transformation.

## 2.3. Transformation algorithms

Once correspondence points had been established, one of a variety of transformations was applied to align the histology image to the macroscopic tissue photograph. For this study, transformations were non-warping corresponding to rotation,  $x$  and  $y$  displacements, and uniform scaling; polynomial; triangle-based, and thin-plate splines (TPS) transformations. For each transformation we obtain a mapping

$$g[x, y] = f[x', y'] = f[a[x, y], b[x, y]], \quad (1)$$

where  $g[x, y]$  represents the pixel in the output image at coordinate  $(x, y)$  and  $f[x', y']$  is the value at  $(x', y')$ , a real-valued location in the input image. The only difference between transformations are the functions  $a[x, y]$  and  $b[x, y]$  that accomplish the mapping. In general, to perform a transformation, we determine parameters in the functions  $a[x, y]$  and  $b[x, y]$  from correspondence points. Then, for each  $(x, y)$  location in the output image, we compute  $(x', y')$  in the input image. To obtain appropriate values at real-valued locations in the input image, we most often use bilinear interpolation. In the triangular-base warping method, quintic interpolation is used. This transformation process is the *inverse* one identified by Wolberg [25]. Details of the transformation equations and parameter estimation follow.

Non-warping registration (NWR) includes  $x$  translation,  $y$  translation, rotation, and uniform scaling. We create this transformation using the standard homogeneous matrix formulation [26]. With many correspondence points, parameters are overdetermined, and a least squares approach is used that corresponds to minimizing the Euclidian distance between correspondence points. Once parameters are obtained, the transformation is applied.

For polynomial warping, we used cubic polynomials in  $x$  and  $y$  to specify the spatial transformation

$$x' = \sum_{i=0}^3 \sum_{j=0}^3 Q_{ij} x^j y^i, \quad (2)$$

and

$$y' = \sum_{i=0}^3 \sum_{j=0}^3 R_{ij} x^j y^i, \quad (3)$$

where the  $Q$ 's and  $R$ 's are the four polynomial coefficients. Coefficients were again determined using least squares estimation, requiring a minimum of 16 pairs of points.

We used the *triwarp* function of IDL to implement warping with triangular patches. Briefly, a Delaunay triangulation is performed on the irregular grid of coordinates for both images. The output of triangulation is a set of corresponding triangular patches between the images. To warp, the algorithm matches vertices of corresponding triangle patches, and then interpolates the data within the triangle using Akima's quintic polynomials [27]. Extrapolation is required to obtain pixel values outside boundary triangular patches, and Akima's extrapolation method is used. Smooth transitions between triangular patches are obtained using partial derivatives in the 'global method' described by Renka and Cline [28].

The TPS algorithm is described by Bookstein [29] and implemented using the algorithm described by Davis et al. [30]. The TPS warp is based on the deformations of a thin metal plate, and provides a smooth, continuous transformation. TPS does not involve a least squares solution; instead it is an interpolating function, which guarantees that correspondence points match exactly.

## 2.4. Tissue section tears

An advantage of our interactive method is that we can correct tears in a histological sample. Tears can be partial where the tissue splits, often creating a V shaped opening, or complete where the tissue is severed into two parts. If the tear occurs in an unimportant region far from the ablated tissue, then we can simply ignore it, i.e. we use correspondence points from the rest of the tissue and omit any in the torn region. In some situations, we found it necessary to correct a tear. Reconnecting tissue sections involved several steps and required a TPS warp. A detailed description of an example is given in Section 4.



### 3. Experimental methods

We conducted experiments to optimize the algorithm and to determine our ability to correct distortion in histology images. We first describe the experiments for algorithm optimization and evaluation methods. We then describe methods for tissue handling and image acquisition. Finally, we describe an example application in RF thermal ablation.

#### 3.1. Experiments for algorithm optimization

We performed experiments to determine the best transformation method and the number and type of correspondence points required. There were three independent variables. First, we varied the number of points in boundary segments. Typically four to six pairs of boundary segments were identified. Depending on the length, each border segment was divided into eight to sixteen points having an equal distance between them of about 1–2 mm. This gave 40–60 total boundary points per tissue sample. To examine the effect of the number of boundary points, we reduced the number to one half and one fourth of the original number by skipping one and three points, respectively, giving three conditions: full (40–60), half (20–30) and a fourth (10–15). Second, we varied the number of internal points used. Pairs of internal correspondence points were identified from the ink fiducials. Zero, one, two, three, or four internal correspondence points were used for each transformation. Third, we used the four different transformation methods identified previously. In experiments, we tested each combination of these three independent variables in order to optimize algorithm parameters.

#### 3.2. Evaluation of warping registration

Registration quality was evaluated using both quantitative error metrics and qualitative visual inspection. For quantitative evaluation, three to five internal ink marks were exclusively used as validation points. Following a transformation, we obtained the  $x$  offset,  $y$  offset, and Euclidean distance between each pair of validation points. This data was analyzed using graphical and standard statistical techniques. We often averaged the values in an image and called it the validation point error. In addition to calculating an internal error metric, we devised a method to examine how closely borders were aligned after a transformation. Half of the boundary correspondence points were used as control points during the transformation, and the remaining half were used to evaluate the transformation.

Using RegViz, a program written in IDL and created in our laboratory, several visualization methods were used to examine the registration quality. Images were displayed on a monitor for side-by-side comparison. Validation points could be overlaid on the images. The registration of various image features was easily determined using a linked cursor.

That is, when one moved a cursor in an image, a matching cursor was moved in the other image. It was also possible to mark points and curves on structures in the reference image using a free hand drawing tool. These marks could then be copied to the other image for comparison. This method was found to be particularly useful. The program also allowed for overlaying of the two images in different colors. To examine the extent of warping, a checkerboard grid was sometimes transformed using the same parameters for the image transformation.

#### 3.3. Tissue slicing and acquisition of calibrated tissue images

In experiments, we used macroscopic tissue images as a reference since this enabled us to characterize the deformation that occurs from histological processing alone. For testing, we used three formalin-fixed sheep brains (Nebraska Scientific, Omaha, NE).

We obtained 4 mm tissue slices using a specially designed tissue slicing apparatus. The slicing apparatus was constructed from Plexiglas and included a tissue platform and a linear displacement device (Rack and Pinion Slide, Edmund Scientific, Barrington, NJ) for accurate stepping of the tissue platform in small increments. We sliced each brain specimen with a 12.8 in. autopsy knife (Tissue-Tek Accu-Edge Semi-Disposable Autopsy Knife System, Sakura Finetek, Japan) using the two vertical supports of the slicing apparatus as a guide. Repeatedly, we sliced the tissue face and advanced the platform by 4 mm until the specimen was traversed. We then cut each thick-sectioned tissue slice to fit a  $2.5 \times 7.5$  cm histology-mounting block.

Ink fiducials were added to each tissue sample to ensure that corresponding points could be located in both the macroscopic tissue and histological images. We used pins dipped in colored inks (Davidson Marking System, Bradley Products, Bloomington, MN) for histological marking. Pins were inserted into the tissue sections at three to five points around the outside boundary and seven to eight points in the interior of the tissue sample. The pins with large color-coded heads were left in the macroscopic tissue sample for photographing. This was done because ink marks were sometimes not circular and difficult to identify in these images. The head of each pin gave a 2 mm diameter disk in the image that enabled us to accurately locate the center of the pin.

After placing the pins in the tissue sections, we photographed them using a digital camera (DSC-D770, Sony, Japan) mounted on a copy stand. Fig. 2a shows a typical image containing the ink fiducials. To prevent any foreshortening in the tissue photographs, we created a method to ensure that the imaging plane of the camera was parallel to the tissue face. A straight pipe was placed on the copy stand perpendicular to the plane of the tissue face. Using the camera's display to view the shaft of the

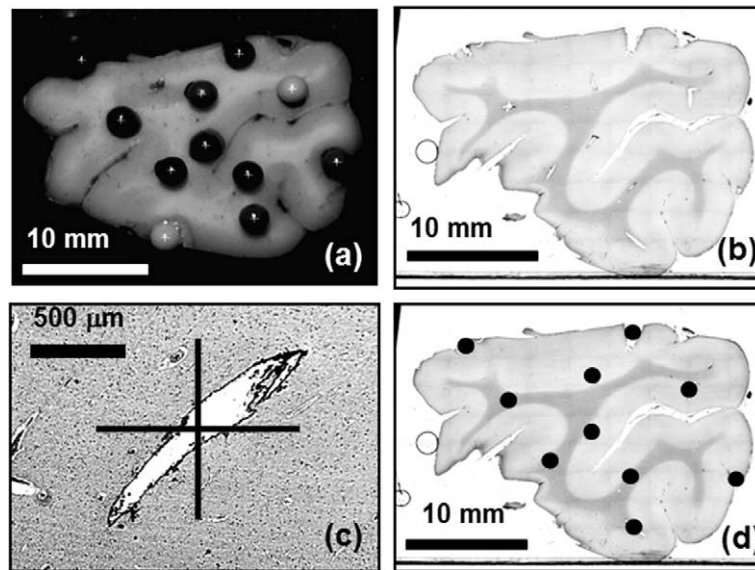


Fig. 2. Determination of pin fiducial locations in macroscopic tissue and histological images. Images are from a sheep brain. From the macroscopic tissue image (a), centroids of pinheads are obtained and used as correspondence points. Pins are removed and the tissue section is processed to create H&E stained slides that are digitized to create a map image (b). To detect ink marks, the slide is viewed at high magnification ( $40\times$  in this case) in a live video window with a digitally imposed centered crosshair (c). The ink mark is centered under the crosshair, and the position of the stage is used to determine the location of the ink mark. Ink marks are superimposed on the digitized map histology image (d).

pipe, the camera was rotated until the front and back openings of the pipe were centered, and then it was secured with a locking screw. We calibrated these macroscopic tissue images using a ruler in the plane of the tissue slice. The tissue images yield square pixels that were typically  $60\mu\text{m}$  on a side. Ink fiducial locations in macroscopic tissue images were found by calculating the centroid of each pinhead.

After the tissue was marked and photographed, we obtained histological samples. We embedded the fixed tissue samples in paraffin, cut three to five  $5\mu\text{m}$  thick sections from the paraffin block near the photographed tissue face and parallel to the tissue images, affixed them to glass slides, and stained them with hematoxylin and eosin (H&E). A total of 10 sheep brain sections were processed using the above procedure.

### 3.4. Acquisition of histological images

We digitized the histology slides using a video microscopy system with a motorized stage. The system consisted of a light microscope (BX60, Olympus, Japan), video camera (DXC-390, Sony, Japan), video coupler (U-TV0.35XC, Olympus, Japan), position encoded motorized stage (ProScan, Prior Scientific, Rockland, MA), and software (Image-Pro with Scope-Pro, Media Cybernetics, Silver Spring, MD). To obtain an image of the entire slide, we used the tiling function of Scope-Pro. This procedure drove the motorized stage, acquired a series of pictures, and seamlessly combined the photographs to form one large tiled image. We performed tiling with a  $4\times$  objective.

Typically, the tiled image consisted of about 100 image acquisitions over a  $3.0\times 2.5\text{ cm}$  tissue sample and gave about  $6400\times 4800$  square pixels that were  $5.2\mu\text{m}$  on a side. Using bilinear interpolation to downsample, the file size of the tiled image was reduced to approximately 10% of its original size to create a smaller map image (approximately  $2024\times 1518$  square pixels that were typically  $16.5\mu\text{m}$  on a side) on which we marked the locations of ink fiducials. This map image, as shown in Fig. 2b, was aligned to the macroscopic tissue image.

A special procedure was required for locating ink fiducials in histology images. Ink fiducials were not always visible in the histology map image (Fig. 2b), but were clearly visible at higher levels of magnification (Fig. 2c). Using the scripting language for Image-Pro and Scope-Pro, we developed software that allowed us to interactively determine locations of ink fiducials. The user panned the slide using a joystick-controlled motorized stage while viewing a live video window. Once a fiducial was found, it was centered under a digital crosshair superimposed on the live image. The user then clicked graphical user interface buttons to record the position of the stage and the objective in use. Instead of using the live video window, one could also view the slide through the microscope eyepiece, which contained a centered crosshair reticule for positioning. When a fiducial was marked, its position was displayed on the map image, which was always displayed on the monitor for reference. Fig. 2d shows the updated histology image with ink fiducial positions shown as black dots. For each ink fiducial, the  $x$  and  $y$  pixel location in the map image was saved to a text file.

### 3.5. Example application of RF ablation in pig model and MR imaging

Following a protocol approved by the Institutional Animal Care and Use Committee, we created *in vivo* thermal lesions in pig kidneys. Using a clinical 0.2 T C-arm MR imaging system (Siemens MAGNETOM OPEN, Erlangen, Germany) for guidance, we inserted an MR-compatible 17-G titanium RF electrode with a 10 mm exposed tip (Radionics, Burlington, MA) percutaneously into the pig kidney. Lesion formation was achieved by increasing the local tissue temperature with resistive heating by delivering RF electric current between the electrode tip and ground pads. We applied RF energy for 10 min using a 100 W RF generator operating at 500 kHz (RFG-3C, Radionics, Burlington, MA). The tip of the RF electrode was maintained at a temperature of  $90 \pm 2^\circ\text{C}$  using a thermistor within the electrode tip. The RF electrode was removed from the thigh before imaging to prevent MR image artifacts.

Approximately 10 min after the ablation, we acquired an MRI volume of the kidney. A T2-weighted turbo-spin-echo sequence was applied with TR/TE/NSA parameters of 3362/68/8 that gives  $256 \times 256 \times 9$  voxels over a  $180 \times 180 \times 27$ -mm field of view (FOV) to yield  $0.70 \times 0.70 \times 3.0$ -mm voxels oriented to give the highest resolution for slices approximately perpendicular to the RF electrode. Since prior reports have documented a consistent overall MRI appearance of the thermal ablation zones [3,4,5,7], independent of the specific T2-weighted pulse sequence parameters, we used one set of acquisition parameters so as to achieve consistency and reproducibility. The pigs were sacrificed approximately 45 min after the ablation, and the kidneys were excised and fixed in 10% formalin for 14 days. The formalin was refrigerated at approximately  $6^\circ\text{C}$  to prevent deterioration of the tissue prior to fixation.

After the kidneys were fixed, we acquired *ex vivo* MR image volumes that documented any deformation from fixation. After each kidney was secured to the tissue platform of our customized slicing apparatus as described above, we placed the apparatus in the gantry of the MR imaging system. A T2-weighted turbo-spin-echo sequence was applied with TR/TE/NSA parameters of 3360/60/10 that give  $512 \times 512 \times 18$  voxels over a  $180 \times 180 \times 27$ -mm FOV to yield  $0.35 \times 0.35 \times 1.5$ -mm voxels. To ensure the tissue-slicing plane and the plane of the MR image slices were parallel, the MR imaging plane was oriented parallel to the two vertical supports of the apparatus that are used as slicing guides. This image volume proved to be useful, especially in the case of the pig kidney, where the *in vivo* images had lower resolution. With an *ex vivo* image volume, we were able to see more detail in the area of the thermal lesion. After the *ex vivo* MR images were acquired, we sliced the tissue, acquired histological samples, and aligned them to the *ex vivo* MR images using the method described in previous sections.

## 4. Results

### 4.1. Registration of histology images

In Fig. 3, we compare non-warping registration (NWR) and a TPS transformation on a histology image. The boundaries of the macroscopic tissue image (a) and the original histology image (b) were first segmented into five corresponding border segments from which 20 pairs of correspondence points, marked by squares, were obtained.

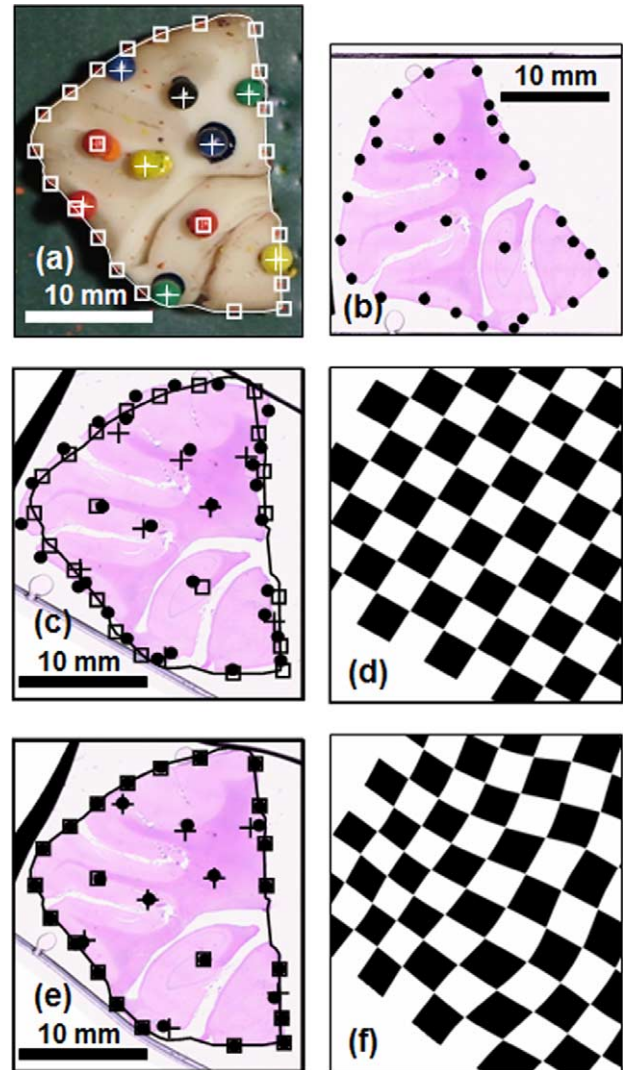


Fig. 3. Registration using the non-warping (NWR) and thin plate splines (TPS) transformation methods. The macroscopic tissue image of a sheep brain is shown with pins and correspondence points as squares (a). The H&E stained histology image is shown with correspondence points identified with small circles (b). Transformations were applied to the histology image to align it with the macroscopic tissue sample using 20 boundary and two internal correspondence points. NWR and TPS results are shown in (c) and (e), respectively. Using the interior points marked with a cross in (a) as validation points, we determine average distances of 0.62 and 0.32 mm for NWR and TPS, respectively. The external boundary aligns with TPS better than with NWR. The same transformations were applied to checkerboard grids to show the effect of warping for NWR (d) and TPS (f).



In addition, two internal points marked with squares were used. In image (c) the non-warping transformation of the histology image shows good alignment with internal validation points (compare the black points with the crosses), but boundary points did not match nearly as well (compare the black points with the open squares). Following a TPS warp (e) using the same set of correspondence points, both the internal validation points and the border points match very well. To demonstrate the amount of warping, we applied the transformations to a checkerboard pattern and displayed the results in (d) and (f). The non-warping result (d) clearly shows that the transformation uses only rotation and translations to align the image while the checkerboard pattern in (f) shows the warping from TPS. For NWR (c), the distance between the three internal validation points was  $0.6 \pm 0.4$  mm. For the TPS warp (e), it was  $0.3 \pm 0.1$  mm. In general, we found several instances where a non-warping transformation reasonably aligned internal markers; however, warping transformations tended to better match the edges of the tissue.

Experiments showed the importance of adding internal correspondence points, especially for those samples where corresponding border segments could not be defined along the entire tissue boundary. Fig. 4 shows the improvement obtained by adding internal points for various transformation algorithms. Three corresponding border segments were identified along the dotted line shown in the macroscopic tissue (a) and histology (b) images; a corresponding border segment could not be located along the bottom edge. No internal correspondence points were used in the transformations on the left, but two internal correspondence points were used in the transformations on the right. Polynomial (c,d), TPS (e,f), triangle (g,h), and non-warping (i,j), transformations were applied. There are several transformations, most often on the left, that we consider to be failures. In such cases, interior validation points in the histology image identified by black dots did not match the crosses from the macroscopic tissue images, and/or internal and external boundaries from the macroscopic tissue image identified as thin black contours did not match corresponding structures in the histology image. All transformed images in the left column, except NWR, failed badly. For these failed transformations, the error of internal validation points ranged from 1.7 to 7.5 mm. By simply adding two internal correspondence points in the right-hand column, transformations improved dramatically; internal validation point errors were between 0.5 and 1.2 mm, and visual alignment of borders improved correspondingly. Despite excellent alignment throughout almost the entire sample, there is often imperfect matching at the bottom edge. The reason is that there was a lack of correspondence points there. In our thermal ablation application, we often do not care about mismatch in areas far from our region of interest.

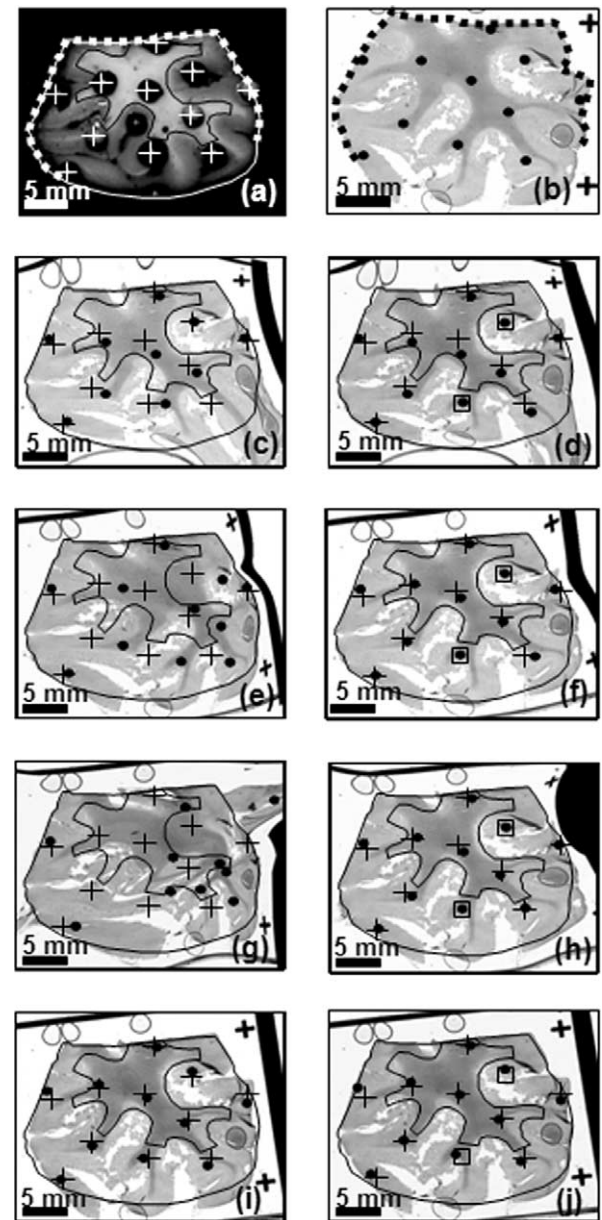


Fig. 4. Comparison of transformation methods and numbers of correspondence points. The reference macroscopic tissue image (a) is shown with external and internal boundaries identified with thin curves. The H&E stained histology image is shown in (b). Interior and boundary correspondence points are shown in (a) and (b). Correspondence could not be identified along the bottom of the sample. The remaining images in the left and right columns contain transformed histology images with boundaries and points from the macroscopic tissue image overlaid. The left column contains polynomial (c), TPS (e), triangle (g), and NWR (i) transformations using 40 boundary points and zero internal points. The right column contains polynomial (d), TPS (f), triangle (h), and NWR (j) transformations using 20 boundary points and two internal points. In general, adding interior points greatly improved the registration. See text for more details.

#### 4.2. Quantitative comparison of algorithms

Initial observations such as those above showed that the visual quality of registration depended upon the



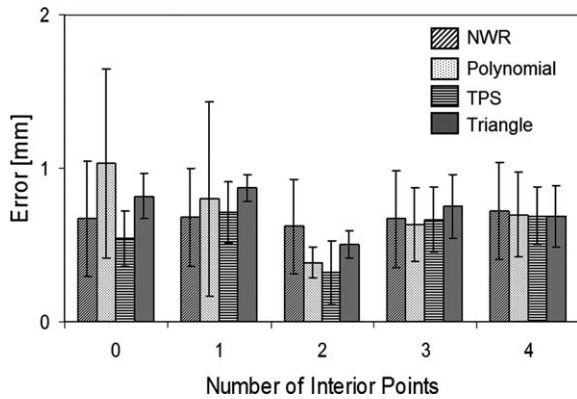


Fig. 5. Effect of adding interior points on transformation methods. Twenty boundary correspondence points were defined along five corresponding border segments. Transformations were applied to the histology image with zero, one, two, three, and four internal correspondence points. Plotted are means and standard deviations over all validation points. For this sample, adding two interior points resulted in the lowest validation point error between macroscopic tissue and transformed histology for all transformation methods.

transformation method, the number and placement of correspondence points, and the tissue section under study. As a result, we decided to systematically investigate algorithm parameters for a variety of tissue sections. We quantitatively evaluated results using the distance between internal validation correspondence points not used in the transformation.

Fig. 5 demonstrates the effect of adding internal control points. A fixed number of 20 boundary correspondence points were defined along five corresponding border segments and used for each of the four transformation methods. For this sample, two interior correspondence points resulted in the lowest validation point error for all

transformation methods. Adding more interior points actually tended to increase the error. Note that a single set of three validation points was used for all cases.

In Fig. 6, we systematically investigated changing the number of internal and boundary control points for the four transformation methods under study. Results are combined over the 10 tissue samples under study, and transformations are: NWR (a), polynomial (b), TPS (c), and triangle (d). The distance error between validation points tends to decrease as the number of internal points is increased along the  $x$ -axis. The non-warping transformation was quite robust with all combinations resulting in less than 1 mm error in all cases and an average of  $0.5 \text{ mm} \pm 0.3$  (a). In the case of polynomial transformations (b), the best results occur with 20–30 boundary correspondence points and two or more internal control points. Ten to fifteen border correspondence points provided too few points for the polynomial transformation so that result is not shown. For TPS (c), it is important to add at least one internal point, and this gave errors less than 1 mm in all cases with an average of  $0.6 \pm 0.3$  mm. With triangle (d), the use of 20–30 boundary points or more greatly improved results. Comparing all graphs, NWR and TPS gave the most consistent results. Additionally, the use of 20–30 boundary points and two internal correspondence points give good results for all transformations.

In addition to giving low average error across all slices, a good warping registration algorithm should not fail and work well with every image slice (Fig. 7). We used algorithm parameters identified above as a good compromise, i.e. we used 20–30 boundary and two internal correspondence points. In Fig. 7a, we show results for five individual tissue samples along with the average result across all 10 samples used in this study. For the most part, all transformations tended to give similar results for each of

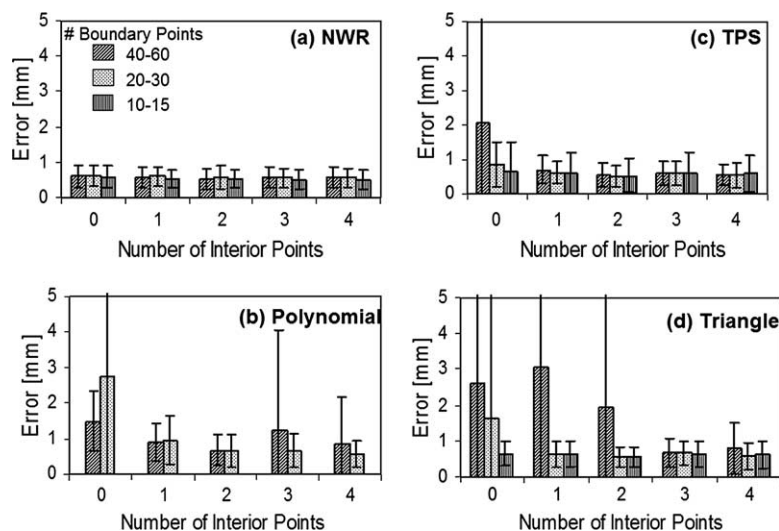


Fig. 6. Effect of the transformation method and number of correspondence points on average registration error as measured by internal validation points. In each panel, the number of internal correspondence points varies from zero to four. The number of border correspondence points varies between 10 and 60 in different bars. Plotted are means and standard deviations over all 10 image pairs. Each image contains at least three validation points, which are averaged together to obtain an error for the image. Algorithms are: NWR, polynomial, TPS, and triangle. Note that with polynomial transformations, 10–15 border correspondence points could not be tested, since polynomial warping requires at least 16 points for the algorithm to work. See text for detailed description.

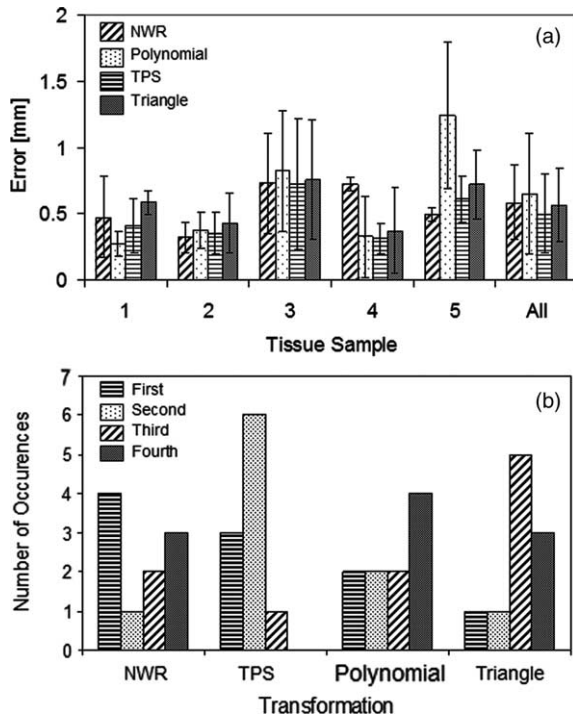


Fig. 7. Registration error is evaluated on individual image slices to examine algorithm robustness. We used good registration parameters identified from Fig. 6, i.e. we used 20–30 border and two interior points. In (a) average distance errors for three, four interior validation points are plotted for all four transformation methods. To reduce clutter, we plot five typical image pairs out of the 10 that were analyzed and plot ‘all’ which is an average over all 10. In almost all cases, the average error is less than 1 mm, and a typical value was around 0.6 mm. For each of the 10 image slices, transformations were rank ordered by error, and the number of first, second, third, and fourth, place rankings were counted for each algorithm and plotted (b). Non-warping registration receives the highest number of firsts with four, followed by TPS with three. While TPS had the second highest number of firsts, it never came in last. Although NWR performed very well in some cases, it came in last three times indicating that it was not very robust.

the tissue samples. Errors all tended to be less than 1.0 mm and were considerably smaller for some samples. The polynomial method gave a relatively large error for tissue sample 5. An alternative way to examine the data is to rank order the transformations according to error (Fig. 7b). TPS gave good results and was very robust; it came in first or second 9 out of 10 times and had no fourth place finishes. Although NWR came in first four times, the most of all methods, it came in fourth 3 times. Recall that the errors in Figs. 5–7a are obtained from distances between corresponding internal validation points and that they do not reflect error at the boundaries.

Errors at boundaries were computed for NWR and TPS by using every other correspondence point as a control point for the transformation and using the remaining points as validation points for the error calculation. Using the best combination, 20–30 boundary and two interior points, gave boundary errors of  $0.03 \pm 0.06$  mm for TPS and  $0.70 \pm 0.60$  mm for NWR. This shows the ability of TPS to correct for boundary distortion and maintain internal structures,

while NWR only works well for the interior of the tissue sample. This observation is evident visually in Figs. 3 and 4.

#### 4.3. Correction of tissue tears

Our interactive method with TPS warping can be used to correct images even when the histology specimen is torn

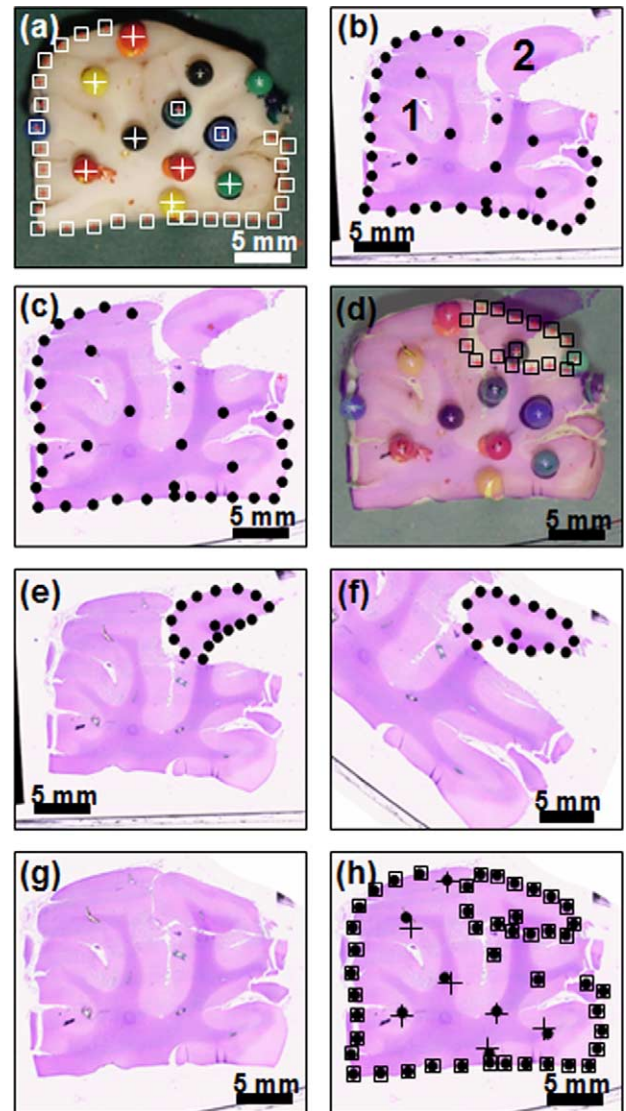


Fig. 8. Registration of histology sample that was torn into two pieces. Several steps are required to register the torn histology image (b) with the reference macroscopic tissue image (a). Correspondence points for the largest piece of tissue are marked by squares and dots in (a) and (b), respectively, and used to transform it with TPS in (c). The transformed image (c) is overlaid on the macroscopic tissue image (a) to create a transparency view (d). Correspondence points are now identified for the small piece of tissue in (d) and (e), and TPS is used to transform it as shown in (f). Note that the rest of the image is distorted because the transformation for the small piece is completely different from that for the larger piece. Finally, the transformed large and small tissue pieces are combined in a single image (g). Overlays from the macroscopic tissue sample, squares and crosses, were added to the final histology image to demonstrate good alignment of points. See text for a more complete description.



apart (Fig. 8). Reconnecting the two pieces in the histology image (b) to match the intact macroscopic tissue section image (a) required several steps. First, four corresponding border segments were found for the largest part (piece-1) of the tissue sample and divided into 26 equidistant points, as shown by the squares in the macroscopic image (a). Histology piece-1 was transformed using TPS (c). To enable the identification of correspondence points for piece-2 along the break, the transformed piece-1 image was combined with the macroscopic tissue image creating a transparency view (d). Correspondence points were then found between the transparency view (d) and histology piece-2 (e). Piece-2 was also transformed with TPS (f). By combining the two transformed pieces, a complete histology image was created (g). Visually, structures align well in the final image (h). Internal validation points, shown by crosses and squares, matched well, and the error was  $0.4 \pm 0.3$  mm. For repairing tears, TPS is used because it results in better final images than other transformation algorithms. In particular, NWR and polynomial warping perform poorly when trying to repair tissue breaks because of the presence of severe distortion.

#### 4.4. Application to iMRI thermal ablation

We applied our method to the analysis of MRI guided RF thermal ablation image data (Fig. 9). The goal was to compare cell damage from histology to signal changes seen in MR images following thermal ablation. The histology image (b) was aligned to the ex vivo MR image (a) using our method. Within the histology image we identified four major zones. Zone 1 (c) is central to the lesion and consists of an empty cavity around the RF needle track. Zone 2 (d) surrounds zone 1 and is characterized by shrunken nuclei, collapsed tubules, and a disorganized tissue architecture. Shrunken cells, hemorrhage, and a high density of extracellular space characterize zone 3 (e). Lastly, zone 4 (f), which is outside of the lesion area, consists of normal kidney cells. To compare this zonal response to the MR images, we copied the boundaries marked in the histology images to the registered MR images. We find that zone 2 corresponds to a region of depressed signal in MR. The reduced signal is possibly due to the shrunken nature of the cells and reduced fluid in the area. Zone 3 corresponds to an increase in MR signal. Most likely, zone 3 is an area of inflammatory response and edema with large extracellular spaces for fluid accumulation. Based on preliminary findings, the boundary of increased signal in MR corresponds to the boundary between healthy and damaged tissue.

## 5. Discussion

Since the spatial distortion found in histological samples is variable, it is critically important to evaluate the best

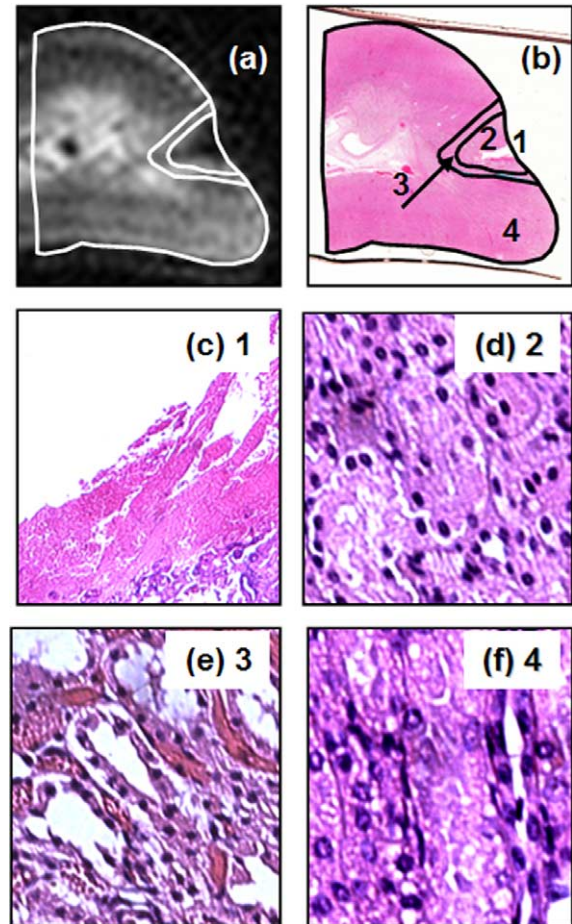


Fig. 9. We applied our method to analyze interventional MRI (iMRI) guided thermal ablation images. The histology image (b) was aligned to the ex vivo iMRI image (a) using our method of a TPS transformation with 20 boundary and two internal anatomical correspondence points. Histology was divided into four major zones as identified in (b), and examples of magnified histology images are shown in (c) through (f) for zones 1–4, respectively. See text for details.

transformation method and the location of correspondence points in systematic experiments. From both visual and quantitative evaluation, TPS is the clear winner, and at least two interior and 20–30 boundary correspondence points are required. This method allows us to correct the distortion near tissue borders, while maintaining accurate matching of internal structures. Perhaps it should be noted that while a transformation obtained from a least squares approach like the polynomial warp can be modified by giving different weights to interior and exterior points, TPS, which exactly matches correspondence points, cannot be adjusted in this manner without modification. Hence, the determination of the number and placement of correspondence points is important. From our experience with a very large number of histology samples from various tissues, we believe that the 10 samples used in this study have representative spatial distortions and that the method is generally applicable.

Interestingly, the non-warping transformation performed very well within the interior of the tissue sample, i.e. in



many cases, NWR did as well or slightly better than TPS for alignment of the interior ink fiducials. However, any differences between the two methods were less than 0.1 mm. While the interior of the tissue is relatively undistorted and can be transformed correctly using TPS or NWR, NWR failed to align the exterior boundary of the tissue where spatial distortions were often more clearly evident. This ability will be quite important in many applications, including RF thermal ablation where the ablation is often applied near the surface of an organ. Similarly, with more interior points, one could express tissue distortion due to local swelling, etc.

TPS appears to express the distortion in histology much better than the other warping transformations. Modifications to warping like creating a biomechanical model of histological distortion or adding a priori constraints such as conservation of volume are probably not applicable. TPS might be as good as any method that one can apply.

The interactive nature of the method allows great flexibility and even allows us to use the method in the presence of tissue tears. In the event of a partial tear far from the region of interest, we can simply ignore the distorted region and not place any control points there. Even a histology sample torn into two parts can be repaired with our method (Fig. 8). Our interactive method is much more accommodating than some automated algorithms such as ones requiring radial correspondence [18].

A source of error has to do with the manual identification of ink fiducials in histology images. Using the centroid calculated from the pinheads reduces the error in corresponding points in macroscopic tissue images. In histology images, one cannot always identify the exact center of ink marks, which often show up as slits in the tissue lined with colored ink (Fig. 2c). Maximum slit size can be of the order of 1 mm, and by choosing the center of the slit, we have a maximum possible error of 500  $\mu\text{m}$ . Using anatomical landmarks could reduce this error, especially in a sample rich with landmarks such as the brain. For boundary points, it might be useful to incorporate automatically determined features of high curvature as correspondence points over limited boundary regions [31].

When the 3D method was applied to iMRI thermal ablation data from pig kidneys, we obtained good correspondence between MR and histology. The voxel to voxel comparison showed both MR and histology exhibit corresponding zonal responses that matched almost perfectly. Near the center of the thermal lesion, histological results showed shrunken, damaged cells which corresponded to a signal reduction in MR. The next zone showed increased MR signal which aligned with areas of increased extracellular space. Also noticeable was the sharp division both in MR and histology between normal and damaged tissue. Our preliminary results using this method indicate that incorporating histological data with MRI can be an important tool for evaluating and improving interventional ablation procedures.

In general, we find the method to be practical and simple to use. Identifying correspondence points is made easier by using ink marks and external borders, and the semi-automatic method gives us flexibility in dealing with distorted and torn tissue samples. When TPS is used with a sufficient number of interior and exterior correspondence points, the method produces corrected histology samples that can be easily compared to macroscopic tissue and MR images.

## Acknowledgements

This research was supported by NIH grant RO1-CA84433 awarded to DLW. We thank Jonathan Lewin for his valuable input and Andrik Aschoff for assistance with pig experiments.

## References

- [1] Breen MS, Lazebnik RS, Lewin JS, Wilson DL. 3D comparison of interventional MR images of radiofrequency thermally ablated tissue with tissue response Proceedings of SPIE medical imaging 2003: visualization, image-guided procedures, and display. vol. 5029 2003 p. 202–9.
- [2] Lazebnik RS, Lancaster TL, Breen MS, Lewin JS, Wilson DL. Volume registration using needle paths and point landmarks for evaluation of interventional MRI treatments. IEEE Trans Med Imaging 2003;22:653–60.
- [3] Aschoff AJ, Rafie N, Jesberger JA, Duerk JL, Lewin JS. Thermal lesion conspicuity following interstitial radiofrequency thermal tumor ablation in humans: a comparison of STIR, turbo spin-echo T2-weighted, and contrast-enhanced T1-weighted MR images at 0.2 T. J Magn Reson Imaging 2000;12(4):584–9.
- [4] Boaz TL, Lewin JS, Chung YC, Duerk JL, Clappitt ME, Haaga JR. MR monitoring of MR-guided radiofrequency thermal ablation of normal liver in an animal model. J Magn Reson Imaging 1998;8(1): 64–9.
- [5] Lewin JS, Connell CF, Duerk JL, Chung YC, Clappitt ME, Spisak J, et al. Interactive MRI-guided radiofrequency interstitial thermal ablation of abdominal tumors: clinical trial for evaluation of safety and feasibility. J Magn Reson Imaging 1998;8(1):40–7.
- [6] Lewin JS, Duerk JL, Jain VR, Petersilge CA, Chao CP, Haaga JR. Needle localization in MR-guided biopsy and aspiration: effects of field strength, sequence design, and magnetic field orientation. AJR Am J Roentgenol 1996;166(6):1337–45.
- [7] Merkle EM, Boll DT, Boaz T, Duerk JL, Chung YC, Jacobs GH, et al. MRI-guided radiofrequency thermal ablation of implanted VX2 liver tumors in a rabbit model: demonstration of feasibility at 0.2 T. Magn Reson Med 1999;42(1):141–9.
- [8] Lee Z, Sodee DB, Faulhaber PF, Lancaster TL, MacLennan G, Wilson DL. Comparison of SPECT and PET imaging for prostate cancer with histological correlation Society of nuclear medicine 48th annual meeting. vol. 294 2001.
- [9] Salem KA, Szymanski-Exner A, Lazebnik RS, Breen MS, Gao J, Wilson DL. X-ray computed tomography methods for in vivo evaluation of local drug release systems. IEEE Trans Med Imaging 2002;21:1310–6.
- [10] Cutler CS, Lewis JS, Anderson CJ. Utilization of metabolic, transport and receptor-mediated processes to deliver agents for cancer diagnosis. Adv Drug Deliv Rev 1999;37(1–3):189–211.

- [11] Runge VM. A review of contrast media research in 1999–2000. *Invest Radiol* 2000;36(2):123–30.
- [12] Chen L, Bouley DM, Harris BT, Butts K. MRI study of immediate cell viability in focused ultrasound lesions in the rabbit brain. *J Magn Reson Imaging* 2001;13(1):23–30.
- [13] Jolesz FA, Bleier AR, Jakab P, Ruenzel PW, Huttli K, Jako GJ. MR imaging of laser-tissue interactions. *Radiology* 1988;168(1):249–53.
- [14] Morrison PR, Jolesz FA, Charous D, Mulkern RV, Hushek SG, Margolis R, et al. MRI of laser-induced interstitial thermal injury in an in vivo animal liver model with histologic correlation. *J Magn Reson Imaging* 1998;8(1):57–63.
- [15] Merkle EM, Haaga JR, Duerk JL, Jacobs GH, Brambs HJ, Lewin JS. MR imaging-guided radio-frequency thermal ablation in the pancreas in a porcine model with a modified clinical C-arm system. *Radiology* 1999;213(2):461–7.
- [16] Likar B, Pernus F. Registration of serial transverse sections of muscle fibers. *Cytometry* 1999;37(2):93–106.
- [17] Kim B, Boes JL, Frey KA, Meyer CR. Mutual information for automated unwarping of rat brain autoradiographs. *Neuroimage* 1997;5(1):31–40.
- [18] Jacobs MA, Windham JP, Soltanian-Zadeh H, Peck DJ, Knight RA. Registration and warping of magnetic resonance images to histological sections. *Med Phys* 1999;26(8):1568–78.
- [19] Toga AW, Ambach K, Quinn B, Shankar K, Schluender S. Postmortem anatomy. In: Toga AW, editor. *Brain warping*. San Diego: Academic Press; 1999. p. 169–90.
- [20] Toga AW, Thompson PM. The role of image registration in brain mapping. *Image Vis Comput* 2001;19(1–2):3–24.
- [21] Mega MS, Chen SS, Thompson PM, Woods RP, Karaca TJ, Tiwari A, et al. Mapping histology to metabolism: coregistration of stained whole-brain sections to premortem PET in Alzheimer's disease. *Neuroimage* 1997;5(2):147–53.
- [22] Schormann T, Zilles K. Three-dimensional linear and nonlinear transformations: an integration of light microscopical and MRI data. *Hum Brain Mapp* 1998;6(5–6):339–47.
- [23] Falcao AX, Udupa JK, Samarasekera S, Sharma S, Hirsch BE, Lotufo RD. User-steered image segmentation paradigms: live wire and live lane. *Graph Model Image Process* 1998;60(4):233–60.
- [24] Mortensen EN, Morse B, Barrett WA, Udupa JK. Adaptive boundary detection using “Live-Wire” Two-dimensional Dynamic Programming. *IEEE Proc Comput Cardiol* 1992;635–8.
- [25] Wolberg G. *Digital image warping*. Los Alamitos, CA: IEEE Computer Society Press; 1992 p. 318.
- [26] Gonzalez RC, Woods RP. *Digital image processing*. Reading, MA: Addison-Wesley; 1992 p. 51–71.
- [27] Akima H. A method of bivariate interpolation and smooth surface fitting for irregularly distributed data points. *Acm Trans Math Software* 1978;4(2):148–59.
- [28] Renka RJ, Cline AK. A triangle-based C-1 interpolation method. *Rocky Mountain J Math* 1984;14(1):223–37.
- [29] Bookstein FL. Principal warps-thin-plate splines and the decomposition of deformations. *IEEE Trans Pattern Anal Mach Intell* 1989;11(6):567–85.
- [30] Davis MH, Khotanzad A, Flamig DP, Harms SE. A physics-based coordinate transformation for 3-D image matching. *IEEE Trans Med Imaging* 1997;16(3):317–28.
- [31] Likar B, Pernus F. Automatic extraction of corresponding points for the registration of medical images. *Med Phys* 1999;26(8):1678–86.

**Michael S. Breen** received the BS degree in electrical engineering from University of Massachusetts Lowell, Lowell, MA in 1990; the MS degree in electrical engineering from Rensselaer Polytechnic Institute, Troy, NY in 1994, and the PhD degree in biomedical engineering from Case Western Reserve University, Cleveland, OH in 2004. He worked several years at Raytheon Corporation in Tewksbury, MA and Picker International (currently Phillips Medical Systems), Cleveland, OH. He is currently a post-doctoral research associate in the Department of Biomedical Engineering at Case Western Reserve University, Cleveland, OH. His research interests include medical image analysis, mathematical modeling of biological systems, tissue typing with medical images and histological verification, and in vivo molecular and cellular imaging.

**Tanya L. Lancaster** received the BS degree in biomedical engineering from Case Western Reserve University, Cleveland, OH. She is currently working at Confirma Incorporated in Kirkland, WA. Her research interests include medical imaging processing and analysis.

**David L. Wilson** received the BS degree in Physics from West Virginia University, Morgantown, WV; the MS degree in biomedical engineering from Penn State University, University Park, PA, and the PhD Degree in electrical engineering from Rice University, Houston, TX. He worked several years at Siemens Medical Systems in New Jersey and Germany. Currently, he is Professor of the Departments of Biomedical Engineering and Radiology at Case Western Reserve University, Cleveland, OH. His active research includes medical image processing, analysis, and visualization, quantitative image quality, and in vivo cellular and molecular imaging.